# Optimized cryo-focused ion beam sample preparation aimed at in situ structural studies of membrane proteins

Miroslava Schaffer[*†], Julia Mahamid[*], Benjamin D. Engel, Tim Laugks, Wolfgang Baumeister and Jürgen M. Plitzko[†]

Max Planck Institute of Biochemistry, Department of Molecular Structural Biology, Am Klopferspitz 18, 82152 Martinsried, Germany

[*] Equal contribution

[†] Corresponding authors: schaffer@biochem.mpg.de, plitzko@biochem.mpg.de

## Abstract

While cryo-electron tomography (cryo-ET) can reveal biological structures in their native state within the cellular environment, it requires the production of high-quality frozen-hydrated sections that are thinner than 300 nm. Sample requirements are even more stringent for the visualization of membrane-bound protein complexes within dense cellular regions. Focused ion beam (FIB) sample preparation for transmission electron microscopy (TEM) is a well-established technique in material science, but there are only few examples of biological samples exhibiting sufficient quality for high-resolution in situ investigation by cryo-ET. In this work, we present a comprehensive description of a cryo-sample preparation workflow incorporating additional conductive-coating procedures. These coating steps eliminate the adverse effects of sample charging on imaging with the Volta phase plate, allowing data acquisition with improved contrast. We discuss optimized FIB milling strategies adapted from material science and each critical step required to produce homogeneously thin, non-charging FIB lamellas that make large areas of unperturbed HeLa and *Chlamydomonas* cells accessible for cryo-ET at molecular resolution.

## 1. Introduction

Single particle analysis by cryo-transmission electron microscopy (TEM) (Frank, 2006) has recently emerged as the method of choice for structure determination of isolated protein complexes (Cheng, 2015; Kuhlbrandt, 2014), enabling the analysis of large, membrane-embedded and flexible macromolecules (Aufderheide et al., 2015; Bartesaghi et al., 2015; Bernecky et al., 2016; Zhou et al., 2015). However, the challenge remains to study the spatial distribution and structural variations of these molecular complexes within their native cellular context (Asano et al., 2015; Mahamid et al., 2016).

Cryo-electron tomography (cryo-ET) provides three-dimensional (3D) views of pleomorphic structures, revealing the menagerie of macromolecules, cytoskeleton and membranes within the cell. In cryo-ET, a tilt-series is acquired by physically tilting and imaging the sample at regular increments, followed by computational reconstruction of these projection images to generate a 3D volume. In order to minimize damage to the specimen, each image in a tilt-series is acquired with low electron dose (~1 $e^-/Å^2$). The resulting low signal-to-noise ratio (SNR) is the major constraint for the detection and interpretation of molecular detail within tomograms (Lucic et al., 2013). Recent advances in instrumentation, most notably direct electron detectors, have made it feasible to attain sub-nanometer resolutions with cryo-ET (Pfeffer et al., 2015; Schur et al., 2015). Phase plates, which are add-on devices mounted in the back focal plane of the objective lens, were developed to improve the contrast in images of vitrified cells (Danev and Nagayama, 2010; Glaeser, 2013). The contrast enhancement is generated by an additional phase shift between the scattered and unscattered electron waves at the diffraction plane. A novel type of thin film phase plate, the Volta phase plate (VPP)(Danev et al., 2014), significantly improves the SNR for the low spatial frequencies, enhancing contrast and facilitating high-resolution imaging at minimal or even zero defocus values (Asano et al., 2015; Fukuda et al., 2015; Mahamid et al., 2016).

The attainable resolution in cryo-ET is directly related to sample thickness. In biological samples thicker than 300 nm, electrons are prone to multiple inelastic scattering events, resulting in image blurring and reduced resolution (Grimm et al., 1997). Zero-loss energy filtering can compensate for these adverse effects, but a general thickness limitation remains. Thus, until recently, molecular resolution could only be routinely achieved for small prokaryotic cells (Nans et al., 2015; Ortiz et al., 2006), the thin peripheries of adherent eukaryotic cells (Medalia et al., 2002) and biochemically isolated organelles (Daum et al., 2010;

Davies et al., 2011; Li et al., 2012; Pfeffer et al., 2015; Pigino et al., 2011; von Appen et al., 2015). With the emergence of cryo-FIB thinning of frozen-hydrated cells (Marko et al., 2007; Rigort et al., 2010b), a wide variety of cell types ranging from larger bacteria to neuronal primary cultures have been made accessible for cryo-ET (Engel et al., 2015b; Fukuda et al., 2015; Hagen et al., 2015; Mahamid et al., 2016; Rigort et al., 2012; Strunk et al., 2012). Ongoing developments hold promise for targeting specific cellular structures (Arnold et al., 2016), even within tissues and multicellular organisms (Hsieh et al., 2014; Mahamid et al., 2015). While FIB micromachining methods allow access to the vast majority of eukaryotic cellular structures, the resulting lamellas of "free-standing" biological material have little contact to the conductive TEM grid. This increases the likelihood of beam-induced specimen movement during TEM imaging. Additionally, electrostatic charging of the specimen can alter the electron wavefront, compromising the use of phase plates (Danev and Nagayama, 2010; Mahamid et al., 2016). Fine metal coating of the final FIB lamella was demonstrated to render the lamellas conductive, allowing the acquisition of tomographic data in combination with the VPP (Mahamid et al., 2016).

Here, we describe a cryo-sample preparation workflow for in situ cellular tomography. We demonstrate how to reproducibly prepare lamellas that exhibit the features required to access molecular-resolution information over large areas (up to 700 $\mu m^2$). These lamellas must be properly vitrified, homogenous in thickness and free of mechanical deformations and surface contamination. To produce such lamellas, the optimized preparation procedure counteracts specimen charging by employing conductive metal sputtering and prevents typical FIB preparation artefacts such as preferential milling and curtaining by additional deposition and milling strategies. Charging during VPP imaging is prevented by coating the final lamellas with a fine conductive metal layer. We demonstrate the application of this workflow to thinning HeLa cells and the photosynthetic single-celled alga, *Chlamydomonas reinhardtii*. The reconstructed 3D tomographic volumes reveal that macromolecular complexes, including those embedded in lipid membranes, can be directly visualized by in situ cryo-ET.

## 2. Results and technical aspects

### 2.1 Sample preparation workflow

In this section, we describe a routine for FIB milling of frozen-hydrated cells to obtain thin, conductive lamellas that are suitable for VPP-assisted cryo-ET (Figure 1). We have previously applied this workflow to

HeLa cell cultures (Mahamid et al., 2016). We begin with a brief introduction of the preparation procedures, followed by discussion of the underlying methodological details.

A basic requirement for cryo-FIB lamella preparation is a vitrified biological specimen. Incomplete vitrification leads to the formation of ice crystals, which can impair both lamella milling and TEM imaging, and in the worst case may cause structural alterations. Thin-film vitrification depends on the cooling rates and specific properties of the biological material. Bigger mammalian cells (e.g. HeLa cells) can be susceptible to crystalline ice formation, but are still amenable to plunge freezing. Throughout the workflow, stable temperature and suitable environmental conditions must be maintained (see supplementary materials) to prevent devitrification (Figure S1) and reduce the introduction of surface contamination, including ice crystals from air humidity during transfers (Figure S2) and water vapor deposition in low-pressure chambers (Figure S1).

The cryo-FIB is used to micromachine cells into lamellas that are thinner than 300 nm by removing the material above and below an area of interest with the Ga ion beam (Figure 2). These areas of interest can be identified for site-specific milling by correlation with 3D fluorescence light microscopy (Arnold et al., 2016). However, to achieve accurate 3D correlation and facilitate SEM/FIB imaging on non-conductive frozen hydrated samples, it is first required to sputter-coat the surface with a conductive material (Pt sputter, see section 2.2). Second, to avoid curtaining during milling, it is best to additionally deposit a protective layer on top of the milling site (Pt GIS, see section 2.2). Using this approach, lamellas spanning 30 μm x 20 μm were routinely produced from single HeLa cells (Figure 3 A).

These lamellas typically contained transparent amorphous ice at the lamella edges. The centers of the cells, however, were incompletely vitrified due to the low heat transfer capacity of the biological material. Furthermore, the lamellas exhibited a thickness gradient along the milling direction, with the thinnest regions towards the tops of the lamellas (Figure 3 A). While this thickness gradient cannot be completely avoided, we present a milling approach to fabricate lamellas containing large areas of uniform thickness (wedge pre-milling, see section 2.3).

Imaging with the VPP requires consistent and robust electron optical settings. Thus, to avoid detrimental electrostatic charging during tilt-series acquisition, this optimized workflow introduces a post-milling metal coating strategy (Pt sputter, see section 2.4). The final step of the workflow is tomographic data acquisition

at thin lamella regions, combining zero-loss energy filtering with VPP-assisted direct electron detection at close to zero defocus (see section 2.5). Here, the tomography tilt range is adjusted to accommodate for the pre-tilt of the lamella (see section 4.4).

VPP-enabled cryo-ET on milled HeLa cells revealed a variety of organelles with molecular detail, including ER membranes, lysosomal compartments, lipid droplets, mitochondria and the cytoskeleton (Figure 3 B). Within the mitochondria, rows of ATP synthase complexes could be seen decorating the native crista membranes (Figure 3 C). Characteristic features of ATP synthase were clearly visible, including the ~10 nm $F_1$ head domain and the stalk that connects $F_1$ to the membrane-embedded $F_0$ domain (Allegretti et al., 2015; Zhou et al., 2015). The lamella that yielded the tomogram in Figure 3 had a thickness of 170 nm, covered by an additional 45 nm of condensed water vapor, followed by a 5 nm conductive layer of sputtered Pt (Figure 3 D).

To consistently obtain lamellas of this and even better quality, we optimized our workflow to include milling procedures that produce large areas of uniform thickness, coating strategies for lamella protection (pre-milling) and conductivity (post-milling) and preventive measures to cope with various sources of contamination. We detail the key requirements for each of the optimized procedures in the following sections. The results are demonstrated on the *Chlamydomonas* mat3-4 strain, selected for this work because its ~5 μm cell diameter is half the size of wild-type cells (Olson et al., 2010; Umen and Goodenough, 2001). This strain generally achieved superior vitrification throughout the entire cell volume, enabling the development of the workflow optimizations.

## 2.2 Pre-milling coating

Two pre-milling coating steps substantially increase lamella quality. A 5-10 nm sputter-coated Pt layer deposited in the FIB prep chamber reduces overall specimen charging. This improves the detection of cellular features in scanning electron microscopy (SEM) images, essential for accurate targeting (Figure 4), especially in combination with correlative fluorescence microscopy (Arnold et al., 2016). This layer also minimizes charge-induced movements during FIB milling, allowing for higher milling precision.

An additional organometallic Pt (trimethyl(methylcyclopentadienyl)platinum(IV)) layer, approximately 2 μm in thickness, is required to protect the sample surface during milling. The cellular cytoplasm contains

areas of different density that cause non-uniform ion beam milling rates, known as curtaining (Figure S2 A, B). Adding a continuous dense layer of organometallic Pt to the top milling surface of the cell greatly reduces curtaining as well as the redeposition of milled material (Figure S2 B). This protective layer is deposited within the FIB chamber using the gas injection system (GIS), following a protocol adapted from Hayles et al. (Hayles et al., 2007). The GIS temperature is set to 26-28 °C, the stage is lowered to 2-3.5 mm below working distance, the sample is rotated towards the GIS needle and the gas flow is opened for 4-8 s depending on the desired layer thickness. The layer must be thick enough (>1 µm) to remain intact during all of the milling steps. However, an overly thick layer (>3 µm) can cause problems during the final milling, as bending of this layer obscures the ion beam trajectory and causes material redeposition on the lamella surface (Figure S2 B, C). While the above experimentally determined conditions yield a layer of reproducible thickness, the reproducibility is affected by precursor gas flow, the distance of the needle from the point of interest and the precision of the manually performed steps.

## 2.3 Cryo-FIB milling

The most routinely employed FIB procedure, which we call "simple rectangular pattern milling", involves stepwise milling at a single tilt angle (within a range of 15°–25° stage tilt) using two parallel rectangular patterns (Rigort et al., 2012). The two patterns on either side of the lamella are milled simultaneously, and the distance between the patterns is reduced stepwise to thin the lamella. The initial rough milling step to produce a lamella of 5 µm thickness is done with a high ion beam current (0.5 nA). The ion beam current is subsequently adjusted to lower values as the thinning progresses (first 0.3 nA for 3 µm thickness, then 0.1 nA for 1 µm thickness). Final cleaning steps are then performed with a low current of 50-30 pA to obtain lamellas thinner than 300 nm (Schaffer et al., 2015). Each of the three steps necessary to produce a single lamella (including rough pre-milling, thinning and cleaning) requires between 5 and 15 min, depending on the amount of material to be removed. Typically, a single lamella can be prepared within an hour and up to 7 lamellas during a FIB session.

However, due the inherent Gaussian profile of the ion beam, this type of milling causes preferential thinning of the top of the lamella, producing samples that are often only thin in the vicinity of the top edge (Figure 3 A). Very thin samples (~100 nm), which are needed to obtain high-resolution molecular information by cryo-ET, therefore require an optimization of the preparation technique.

The preferential milling effect is well known in material science. There, it is counteracted by alternated milling of either side of the lamella, while at the same time slightly tilting the lamella towards the ion beam to compensate for the beam profile (Langford, 2006). These procedures are typically combined with cleaning cross-section patterns to produce smoother surfaces than those obtained by equal area scanning with a regular rectangular pattern. In cleaning cross-section patterns, a rectangular area is micromachined by repeatedly scanning a single line and shifting this line across the area. As this cleaning milling pattern does not yield a useable image signal, the sample must be simultaneously observed with the electron beam throughout the milling process for accurate pattern positioning and assessment of the milling progress. However, this is not feasible for dose sensitive materials such as frozen-hydrated biological specimens. For this reason, we devised an alternative milling strategy to produce lamellas of uniform thickness. The "wedge pre-milling" method developed for our optimized workflow was adapted from Schaffer et al. (Schaffer et al., 2012) and provides the benefits of compensating for the ion beam profile while avoiding the need for constant imaging during the final milling steps (Figure 5). By creating an initial thick wedge-shaped lamella with angles steeper than required to compensate for the beam profile, the final thinning steps can be performed from both sides with two simultaneously milled rectangular patterns, while still yielding a final lamella of homogenous thickness.

The wedge pre-milling routine for a lamella of 20 µm height consists of the following steps (Figure 5): First, a thick lamella is cut from bulk material with 0.3 nA ion beam current (Figure 5 A). Next, the wedge is prepared by tilting each side of the lamella 1° towards the ion beam and milling with 100 pA until the top of the lamella wedge is ~1.5 µm thick (Figure 5 A). The current is then reduced to 50 pA and the angle reduced to 0.5° for milling each side until the top of the wedge is ~600 nm thick (Figure 5 B). At this point, the bottom of the wedge-shaped lamella is typically ~250 nm thick. The final thinning with two simultaneously milled parallel rectangular patterns is then performed with a 30 pA beam current. The distance between the two rectangular patterns is reduced stepwise and single snapshots are acquired with the electron beam between steps to guide the final thinning process (Figure 6). Lamella thickness and homogeneity can be estimated from secondary electron images using an Everhart-Thornley detector (ETD). Charging contrast typically vanishes at thicknesses below 350 nm for 5 kV / 25 pA imaging and 200 nm for 3 kV / 20 pA imaging. Cellular features visible in the charging contrast disappear as the lamella becomes darker and more homogenous with decreasing thickness. Thinning is stopped before the protective Pt layer loses its integrity (Figure 6, right).

This optimized milling procedure results in lamellas with homogenous thickness across their entire length (Figure 7 B). We typically produce lamellas with thicknesses of 60-200 nm, depending on the particular application. The lowest achievable sample thickness is set by the mechanical stability of the lamella, as further thinning could destroy the lamella's integrity. Fabricating a lamella of shorter width (<12 µm) can help to alleviate this problem, but reduces the accessible sample area for subsequent TEM imaging.

## 2.4 Post-milling coating

As the organometallic Pt protective layer applied before milling is not sufficiently conductive, additional coating ensures better conductivity of the FIB-lamellas during cryo-TEM investigation. We have had success with a simple approach of applying a thin conductive coating on top of the finished lamella (Figure 3 C). The layer should continuously cover the lamella surface to render it conductive, while remaining sufficiently thin (<5 nm) to not obscure the native contrast of the cellular specimen during cryo-ET. This is accomplished with a brief Pt sputter (10 mA, 2-3 s) in the FIB-attached prep chamber.

## 2.5 Cryo-ET

Cryo-FIB lamellas are fabricated at an 8°-15° angle with respect to the grid surface (Figure 8). For the most common low-dose acquisition scheme, the focusing area position is shifted along the tilt axis in reference to the exposure location (Figure 8 A). Misalignment of the lamella with respect to the tilt axis results in z-height differences between the focusing and exposure areas (Figure 8 C, D). Variable defocus values at the exposure area will be the direct consequence, with systematic errors that propagate over the course of the tilt-series (Figure S5). These focusing errors are detrimental to achieving stable and comparable imaging conditions, one of the key requirements in tomography.

The contrast-enhancing benefits of the VPP without deterioration of the high-frequency signal can only be harnessed if the image focus is accurately set for each image in the tilt-series, as no CTF correction procedures are currently available for projections acquired with a phase shift (Danev and Baumeister, 2016). While the ideal defocus is close to 0 µm, defocus values of up to 0.5 µm still preserve most of the high-resolution information (~20 Å) in VPP tomograms (Khoshouei et al., 2016). The determined focus value is therefore correct only if both focusing and exposure areas represent the same z-height on the specimen with respect to the electron beam. Thus, a critical aspect of VPP imaging in cryo-ET is the exact lamella

orientation relative to the tilt axis. Correct sample orientation is achieved by precisely mounting the grids into the microscope holder with the aid of visual markers on the Autogrid. To a certain extent, the orientation can also be controlled by rotating the grids on the stage if the sample holder provides this functionality.

VPP-enabled cryo-ET of *Chlamydomonas* FIB lamellas at 0.5 μm defocus revealed the molecular landscapes of native organelles, including chloroplasts, mitochondria, the ER and the Golgi (Figure 9). Densities for numerous different membrane-bound complexes could be distinguished. In the mitochondria, rows of ATP synthase dimers decorated the cristae (Figure 9 A, D), and circular bowl-shaped complexes were found between the inner and outer mitochondrial membranes (Figure 9 C). In the chloroplast, single ATP synthases could be seen bound to thylakoids, while large complexes spanned both membranes of the chloroplast envelope and protruded into the stroma (Figure 9 E). Around the Golgi, we could clearly resolve vesicles encased in coat proteins, including clathrin (Figure 9 F, G) and COPI (Figure 9 B, H). Our ability to image complexes bound to Golgi membranes was not limited to coat proteins, as we previously described a novel structure of arrayed membrane proteins within the trans-Golgi cisternae (Engel et al., 2015b).

## 3. Discussion

The fidelity with which macromolecules can be visually identified in cryo-electron tomograms is dependent on several factors. Foremost is the thickness of the sample volume. Resolution scales with thickness for any TEM investigation. However, a compromise has to be found between what details one would like to see and how big the final tomographic volume should be.

The ability to detect and identify molecular complexes is not limited by thickness alone. The characteristic material properties of various biological samples also have a strong influence. Living cells are inherently crowded, but the degree of molecular crowding can vary greatly from one cell type to another and between different regions within a single cell. Together, a sample's thickness and crowding will ultimately determine the level of detail that can be resolved by cryo-ET. While we can control thickness up to a certain point, we cannot easily control the extent of crowding within living cells. Thus, we must consider the crowding in our cellular region of interest and adjust the lamella's thickness based on the level of detail we would like to resolve in the tomograms.

Our presented sample preparation approach reproducibly yields high-quality lamellas covering large cellular areas of homogeneous thickness, thin enough to directly access molecular-resolution information. Furthermore, it gives us the opportunity to tune the lamella preparation to specific acquisition needs, including VPP imaging. We employed the optimized FIB milling and surface-coating procedures described above for in situ structural studies of HeLa human cells (Mahamid et al., 2016) and *Chlamydomonas reinhardtii* algal cells (Engel et al., 2015a; Engel et al., 2015b). In both of these cell types, we were able to directly visualize and identify membrane proteins within their native environments.

The wedge pre-milling technique (Figure 5) enabled us to fine-tune the lamella thickness (Figure 7). While this procedure is significantly more time consuming (additional 30 min per lamella), wedge pre-milling reproducibly yields the highest quality lamellas, in particular when very thin sections (down to 60 nm) are required. Special care should be taken with regard to the vacuum and relative humidity during the FIB work and transfers (see supplementary material) to avoid condensation of water vapor on the produced lamellas that will add to the effective lamella thickness.

As specimen thickness directly correlates with the SNR of projection images, a direct consequence is the effect on the fidelity with which tomograms can be reconstructed. Because no fiducial markers are present within the cell, tilt-series alignment is performed by feature tracking (e.g. IMOD patch tracking), which is more accurate for thinner volumes. To increase tilt-series alignment accuracy, it would be desirable to design a robust protocol for adding fiducial markers to lamellas. It is debatable whether marker decoration by “dipping” lamellas in organic solution is the best possible approach (Harapin et al., 2015), as it introduces additional handling steps and increases the risk of depositing surface contaminants. An ideal protocol might add fiducial markers within the FIB/SEM chamber or adjoining prep chamber without any additional transfer steps.

Thin platinum coating renders the lamellas conductive, leading to reduced sample charging and enabling VPP imaging. Our instrumentation setup for metal sputtering contains only a Pt source. We have not experimented with the quality of alternative metal coatings (e.g. Pt/C and Cr), known to be advantageous in the field of cryo-SEM imaging due to their lower atomic number, smaller grain size and higher conductive properties.

Although using the VPP for tomographic acquisition on FIB lamellas requires additional precision in specimen mounting and alignment, the in situ tomograms acquired from these lamellas resolve the structures of numerous macromolecules, including membrane-bound complexes within their dense native membranes. Membrane proteins still represent the greatest challenge in structural biology, as they are difficult to study in isolation. The unprecedented data quality presented here will enable the direct visual analysis of the position, structure, conformation and interactions of each macromolecule within the unperturbed cell, opening the door to visual proteomics (Asano et al., 2015; Forster et al., 2010).

# 4. Material and methods

## 4.1 Cell culture

HeLa cells stably expressing beta-tubulin:GFP off a BAC and H2B:mCherry off a plasmid were cultured in the presence of G-418 in Dulbecco's modified Eagle's medium supplemented with 10% fetal bovine serum, 2mM L-glutamine and maintained using standard procedures. Cell cycle synchronization was achieved by an initial block using 2 mM thymidine (Sigma-Aldrich Chemie, Munich, Germany) for 18 h, release for 6 h, followed by a second block using 2 µm S-Trityl-L-Cysteine (Enzo Life Sciences, Loerrach, Germany) for 8 h. Mitotic cells were detached from the culture flask by mechanical shake off, and the collected medium was centrifuged at 300 g for 2 min to concentrate the cell pellet.

*Chlamydomonas reinhardtii* strain mat3-4 (Umen and Goodenough, 2001) was cultured in Tris-acetate-phosphate (TAP) medium with constant light (~10,000 lx) and aeration with normal atmosphere. The culture was grown for two days to mid-logarithmic phase.

## 4.2 Vitrification

Four microliters of the HeLa cell suspension or 3.5 µl of *Chlamydomonas* liquid culture (diluted to 500–4000 cells/µl in fresh TAP) was pipetted onto glow-discharged holey carbon-coated copper grids (R 2/1, 200 mesh, Quantifoil Micro Tools, Jena, Germany). Grids were plunge-frozen in a liquid ethane/propane mixture at liquid nitrogen ($LN_2$) temperature using a Vitrobot® Mark 4 (FEI Company, Eindhoven, The Netherlands).

For HeLa cells, the grids were blotted with Teflon sheets (custom made) on both sides and filter paper on the back side. Blotting chamber conditions were set to 37 °C, 90% humidity, blot force 10, 10 s blot time and 2 s drain time. For *Chlamydomonas*, the grids were also blotted from the back side, and the blotting chamber conditions were set to room temperature, 90% humidity, blot force 10, and 9 s blot time. Grids were stored in $LN_2$ until usage.

## 4.3 Cryo-FIB

Two dual-beam FIB microscopes were used for this work: 1) a FIB Quanta 3D FEG (FEI) equipped with a Quorum PP3000T cryo-system (Quorum Technologies, Laughton, United Kingdom) and a homemade 360° rotatable cryo-stage cooled by an open nitrogen circuit (Rigort et al., 2010a); 2) a FIB Scios (FEI) equipped with a complete cryo-system prototyped by FEI, including a rotatable cryo-stage cooled by an open nitrogen circuit. Both systems utilize FEI Autogrid specimen cartridges modified for FIB preparation under shallow milling angles (Rigort et al., 2012). Two plunge-frozen grids were clipped into Autogrids and mounted into a shuttle under $LN_2$ (Rigort et al., 2010b). The shuttle was mounted into the FIB using the cryo-transfer system. Samples were typically first sputter-coated with Pt in the Quorum prep chamber (10 mA, 30 – 60 s) to improve the overall conductivity of the sample. An organometallic Pt layer was then deposited inside the microscope chamber using the in situ gas injection system (GIS, FEI). Coating procedures are described in detail in sections 2.2 (pre-milling coating) and 2.4 (post-milling coating). During FIB operation, samples were kept at constant $LN_2$ temperature. Lamellas were produced using the gallium ion beam at 30 kV with stage tilt angles of 15°-20°, employing procedures described in detail in 2.3 Cryo-FIB milling.

## 4.4 Cryo-TEM and tomography

Cryo-TEM imaging was performed on a Titan Krios (FEI) operated at 300 kV. The microscope was equipped with a field-emission gun, a Quantum post-column energy filter (Gatan, Pleasanton, CA, USA) and a heated phase plate holder (FEI) (Danev et al., 2014). Data was recorded on a K2 Summit direct detector camera (Gatan) operated in dose fractionation mode. Tilt-series images were collected using SerialEM (Mastronarde, 2005). Individual frames acquired for each tilt were aligned according to the procedures developed by Li et al. (Li et al., 2013).

The tilt range for FIB lamella tomography takes into account the pre-tilt of the lamella (8°-15°) and, depending on the direction that the grid was mounted, is typically (±)50° to (±)70°. Tilt-series were acquired with a tilt increment of 2°, an object pixel size of 0.421 nm or 0.342 nm, and a total dose ~60-100 $e^-/Å^2$. Alignment and operation of the VPP were carried out essentially as described by Fukuda et al. (Fukuda et al., 2015). The target defocus was set between 0 and -0.5 μm. The tomographic tilt-series presented in this report were collected using standard automated acquisition procedures within SerialEM. Special care was taken to properly align the lamella's pre-tilt axis parallel to the tomographic tilt axis to avoid tracking and focusing errors (described in Section 2.5).

## 4.5 Tilt-series image processing

Tilt-series alignment and tomographic reconstruction was performed using version 4.7 of the free IMOD software package (Kremer et al., 1996). Alignment of tilt-series projection images was performed with IMOD patch tracking because no gold nanoparticles were available within the cell volumes as fiducial markers. Final alignment of the tilt-series images employed linear interpolation and a low pass filter (cut off: 0.35, sigma: 0.05). No CTF correction was performed on the phase plate data. For tomographic reconstruction, the radial filter options were left at their default values (cut off: 0.35, fall off: 0.05).

## Acknowledgements

We are grateful to Radostin Danev for assistance with VPP operation, to the department's workshop for the design and production of various tools, and to Dimitry Tegunov for the development of the frame-alignment tool. M.S. was supported by the European Commission grant agreement ERC-2012-SyG_318987-ToPAG. J.M. was supported by postdoctoral research fellowships from EMBO and HFSP, and by the Weizmann Institute Women in Science Program. B.E. was supported by a postdoctoral research fellowship from the Alexander von Humboldt Foundation. We also acknowledge support from the Deutsche Forschungsgemeinschaft Excellence Clusters CIPSM and SFB 1035, and the Max Planck Society.

## Figure legends

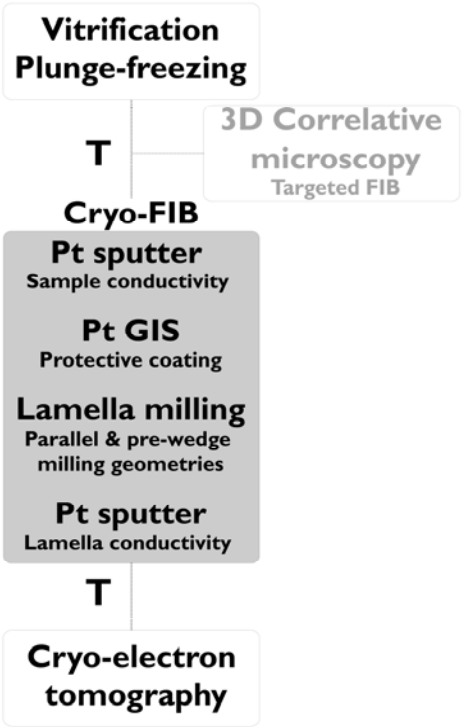


Figure 1. Cryo-sample preparation workflow with adapted FIB milling and Pt coating strategies. All steps in the grey box are performed within the cryo-FIB dual-beam microscope and adjoining prep chamber. T: transfers between instruments; Pt: platinum; GIS: gas injection system.

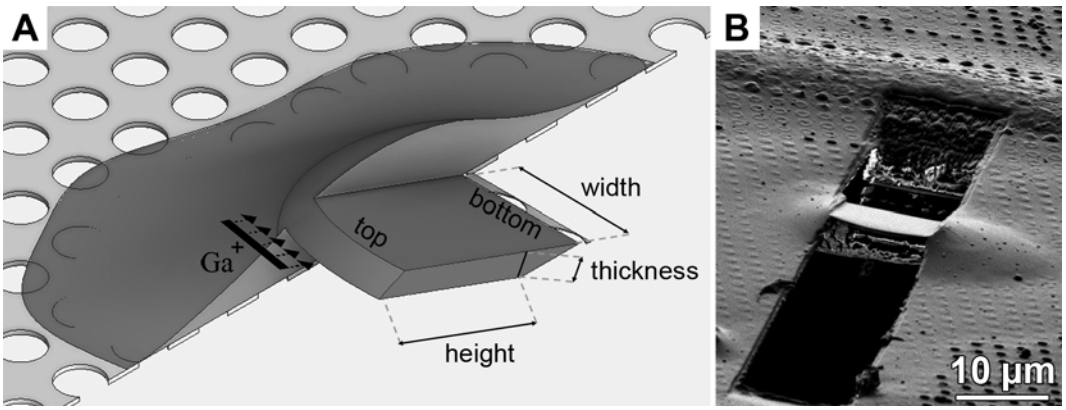


Figure 2. Geometry of FIB lamella preparation. A: Cross-section of a FIB lamella showing the direction of the gallium beam ($Ga^+$) and the terminology of lamella dimensions used throughout the text. B: FIB image of a lamella prepared from a *Chlamydomonas* cell.

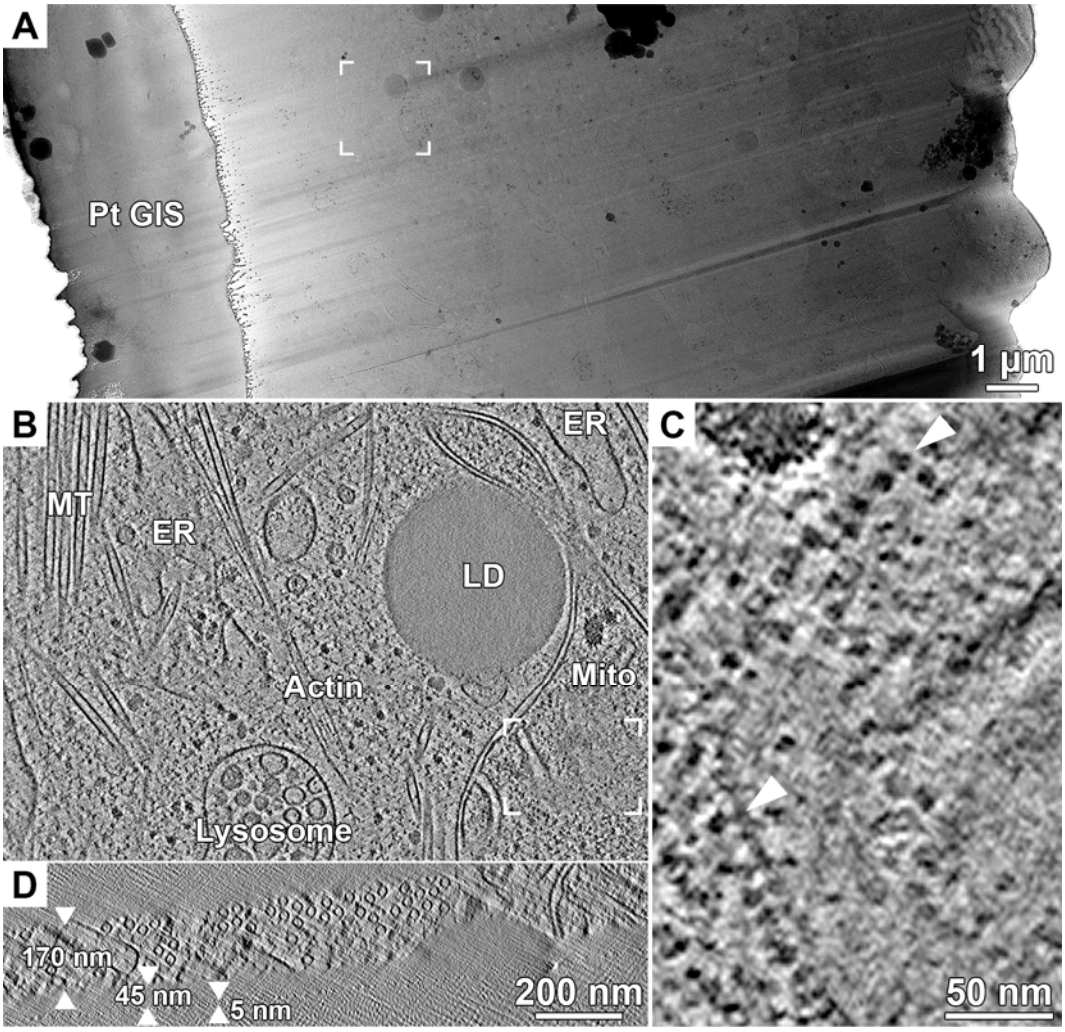


**Figure 3.** Cryo-EM/ET on a FIB lamella of a HeLa cell. **A:** 2D TEM montage of a HeLa cell FIB lamella. Left: lamella top with an organometallic Pt layer. Right: thicker bottom side of the lamella. **B:** x,y slice from a tomographic volume acquired at the framed area in **A**, showing a variety of organelles and cytoskeletal structures within the cytoplasm. MT: microtubules, ER: endoplasmic reticulum, LD: lipid droplet, mito: mitochondrion. **C:** Enlarged area within the mitochondrion (framed region in **B** rotated by 90°). A row of ATP synthase complexes is visible along the cristae membranes in top view (top arrowhead) and in side view (bottom arrowhead). **D:** Corresponding x,z slice of the tomographic volume in **B**. The lamella thickness is 170 nm with a 5 nm Pt surface coating sputtered after lamella preparation. An additional ~45 nm layer of water vapor condensed on the finished lamella over the course of an hour during preparation. Tilt-series was recorded with the VPP, a target defocus of 0 µm and an object pixel size of 0.421 nm.

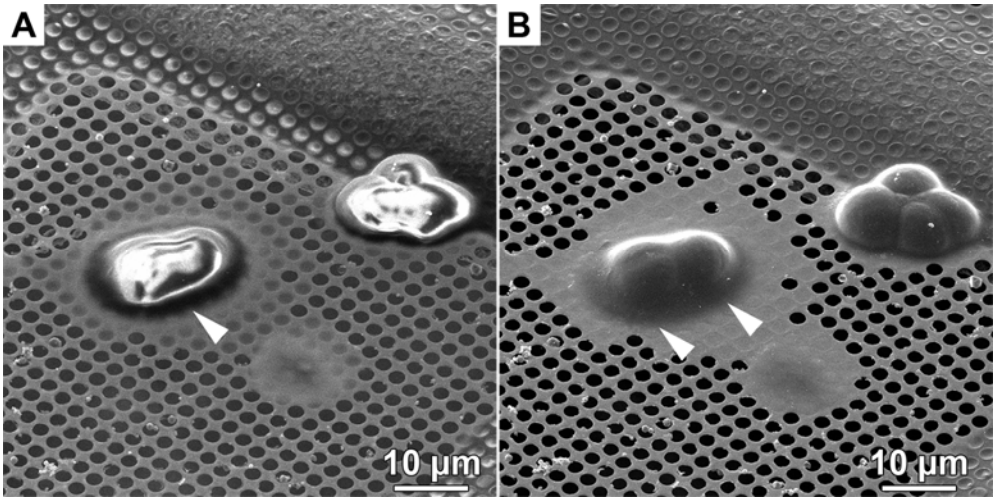


Figure 4. SEM secondary electron images (5 kV, 25 pA) of *Chlamydomonas* cells showing the effect of conductive Pt coating. A: Charging contrast in the uncoated specimen obscures the view of specimen topology. Individual cells are not recognizable (white arrowhead). B: After Pt sputtering, the sample no longer shows charging contrast. Two cells are clearly distinguishable (white arrowheads).

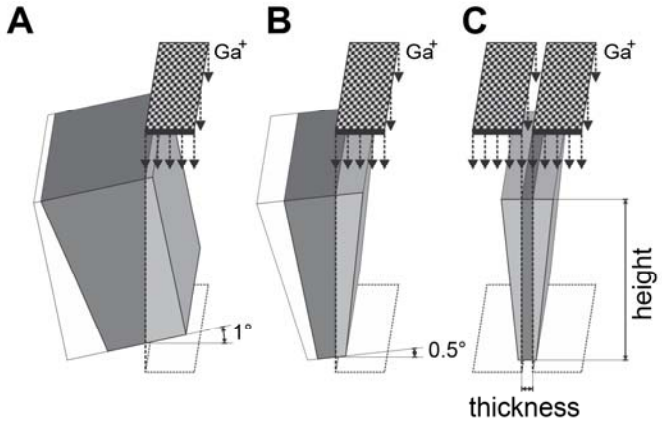


Figure 5. Schematic of the wedge pre-milling steps, drawn with exaggerated angles. The checkered areas represent the milling pattern and the black arrows indicate the ion beam direction. Dark grey represents the lamella, light grey indicates the sample material to be removed during the current step, and white shows previously removed sample material. A: Initial milling at 1° tilt towards the ion beam. This step is repeated for both sides. B: Subsequent milling at a shallower tilt angle of 0.5° with reduced ion beam current. This step is repeated for both sides. C: The final milling steps are carried out at 0° tilt using two simultaneously milled patterns (identical to the final steps of simple rectangular pattern milling). The distance between the parallel rectangular patterns is reduced stepwise until the desired lamella thickness has been reached.

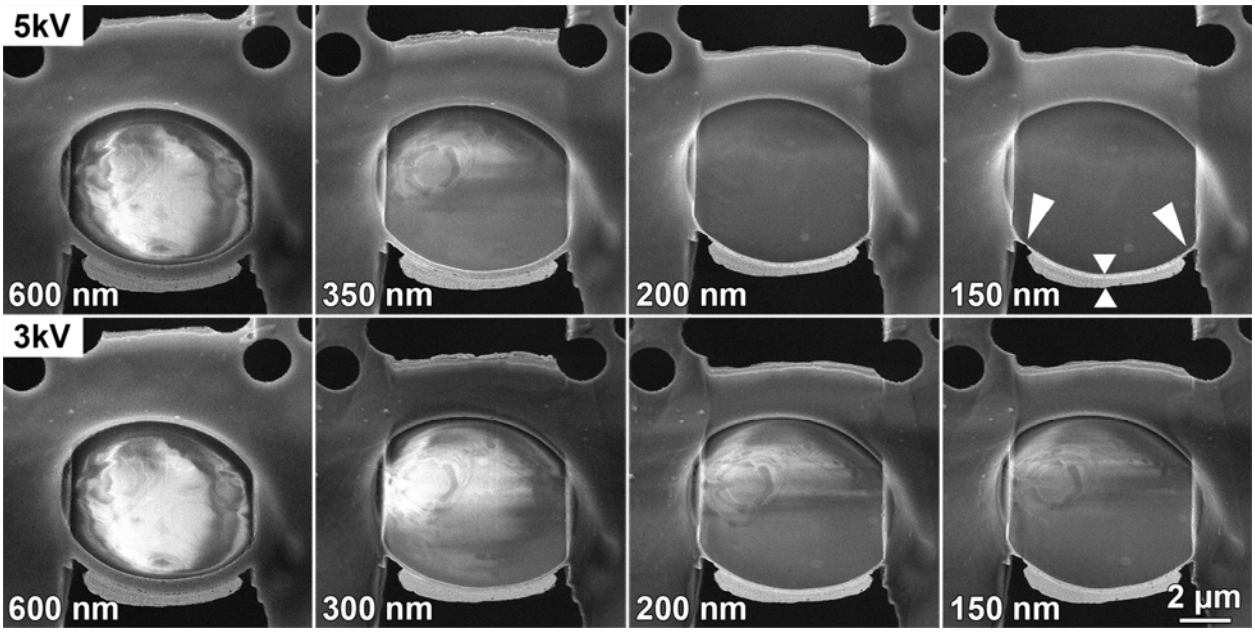


Figure 6. Estimation of sample thickness during FIB milling by thickness-dependent contrast changes in secondary electron images. ETD images showing four sequential final lamella-milling steps (left to right). The lamella thickness is indicated at the bottom of each image. Charging contrast, which reveals cellular features, vanishes when the lamella thickness drops below ~350 nm when imaged with a 5 kV electron beam (top row) but remains visible down to a thickness of ~200 nm when imaged with a 3 kV beam (bottom row). Small arrowheads indicate the protective organometallic Pt layer at the top of the lamella. Milling should be stopped before the integrity of this layer is compromised (large arrowheads).

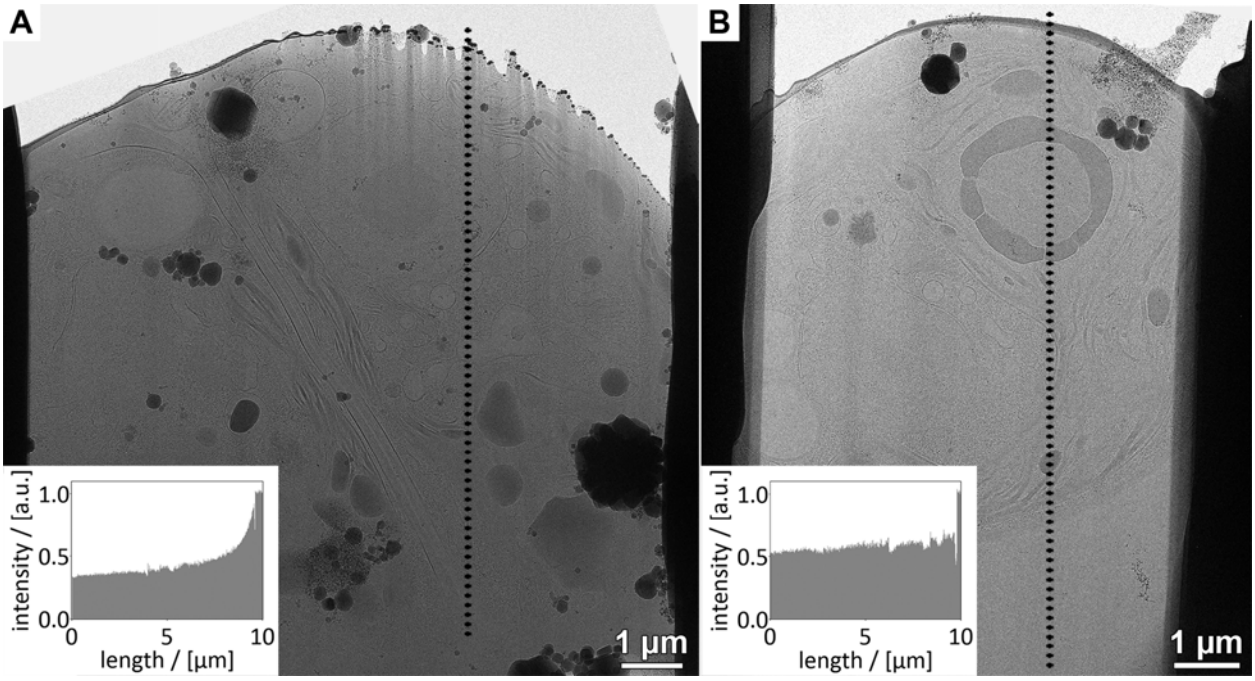


Figure 7. FIB lamellas of *Chlamydomonas* cells. A: Lamella produced by simple rectangular pattern milling. B: Lamella produced by the wedge pre-milling technique, exhibiting a more uniform thickness. Insets: Intensity profiles along the dashed lines, indicating the homogeneity of each lamella's thickness.

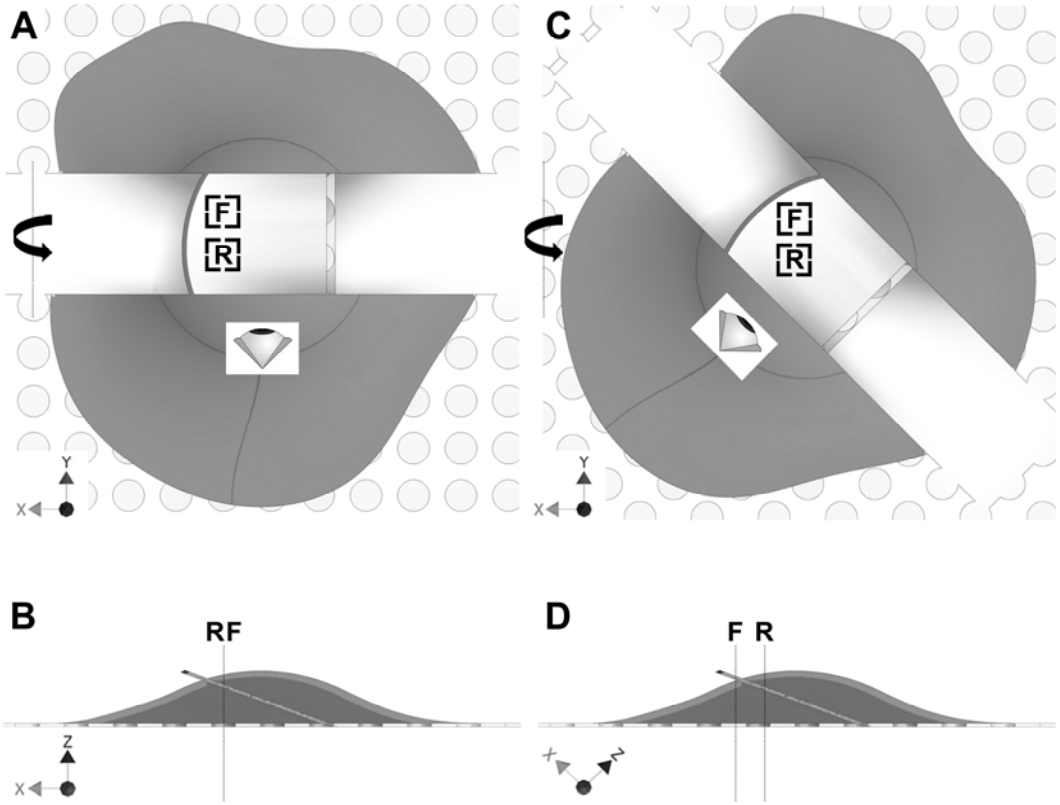


Figure 8: Consideration of FIB lamella orientation with respect to the tomographic tilt axis. A: Correct orientation of the lamella relative to the tomographic tilt axis (black dotted line with turning arrow) results in a focus area (F) at the same z-height as the record area (R). B: Side view of the lamella in A (viewing direction from eye in A) showing the equal heights of F and R when the lamella is properly oriented. C: With incorrect orientation, the focus and record areas are at different heights on the lamella, resulting in a systematic focusing error. The diagram shows the extreme case of a 45° rotation of the lamella relative to the tilt axis. D: Side view of the lamella in C (viewing direction from eye in C), showing that F and R are at different heights on the lamella. The distance between F and R is typically 3 μm at magnifications with object pixel sizes of 0.3-0.4 nm.

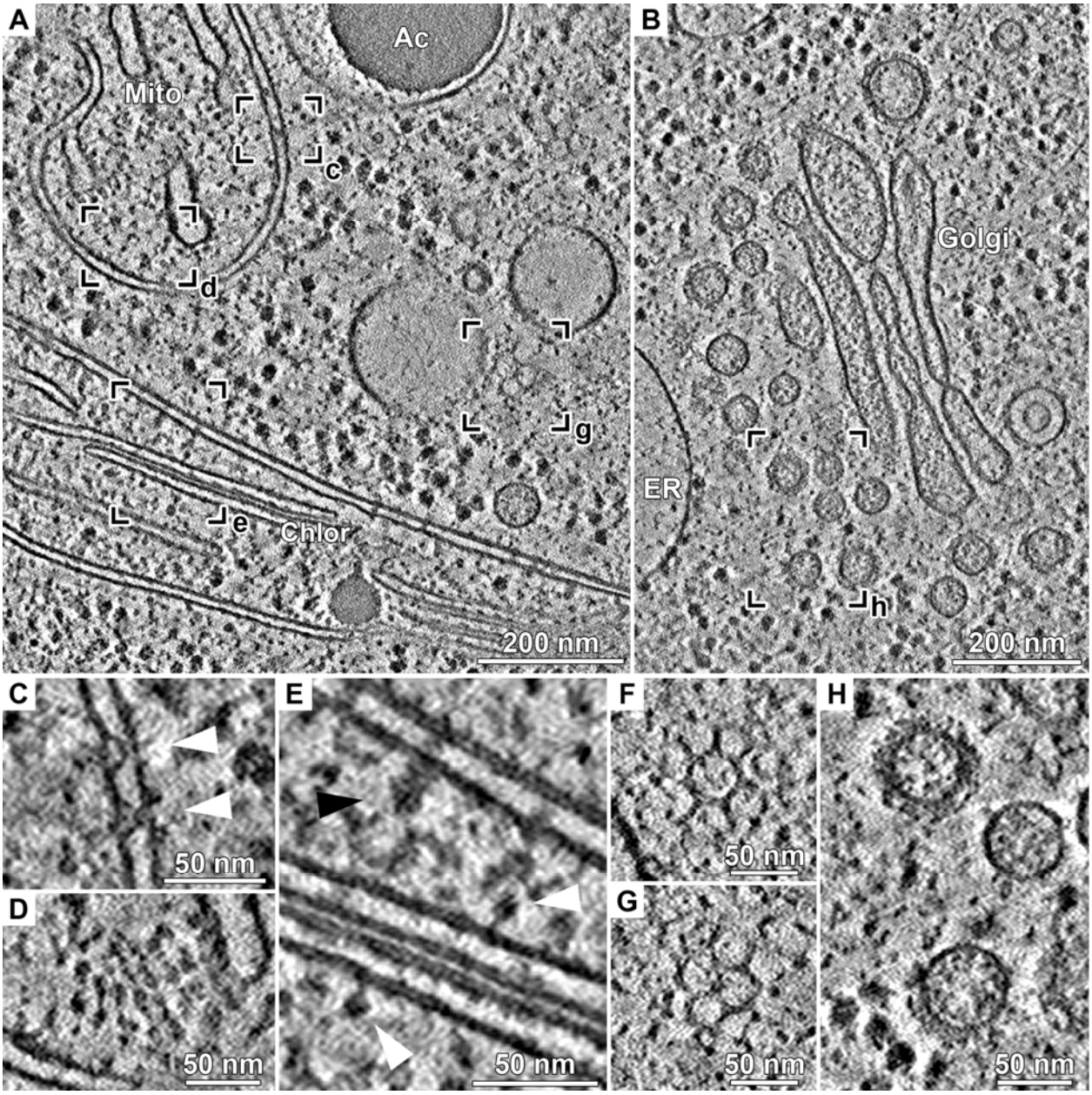


Figure 9. Visualization of molecular complexes within *Chlamydomonas* cell FIB lamellas that were prepared using wedge pre-milling. A-B: Overview slices from tomographic volumes. Mito: mitochondrion, Chlor: chloroplast, Ac: acidocalcisome, ER: endoplasmic reticulum. The framed regions in A and B correspond to the indicated close-up views in C-H. These magnified views show different tomographic slices than those depicted in A and B. C: Circular bowl-shaped complexes (arrowheads), seen as semicircles in this side view, positioned between the mitochondrion's inner and outer membranes. D: Top view of rows of ATP synthase dimers bound to a crista membrane. E: Single ATP synthases bound to thylakoid membranes (white

arrowheads) and a large complex that spans the outer and inner membranes of the chloroplast envelope (black arrowhead). **F-G:** Clathrin coats in the cytoplasm (**F** is from a region of the tomogram in **A** that is not shown). **H:** Vesicles near the cis-Golgi with complete (top), partial (bottom) or no (middle) COPI coats. The lamellas were 140 nm (**A**) and 95 nm (**B**) thick, and each covered with 60 nm of condensed water vapor followed by 5 nm of sputtered Pt. Tomograms were acquired with the VPP, a target defocus of -0.5 μm, and an object pixel size of 0.342 nm.

## References


Allegretti, M., Klusch, N., Mills, D.J., Vonck, J., Kuhlbrandt, W., Davies, K.M., 2015. Horizontal membrane-intrinsic alpha-helices in the stator a-subunit of an F-type ATP synthase. Nature 521, 237-240.

Arnold, J., Mahamid, J., Lucic, V., de Marco, A., Fernandez, J.J., Laugks, T., Mayer, T., Hyman, A.A., Baumeister, W., Plitzko, J.M., 2016. Site-Specific Cryo-focused Ion Beam Sample Preparation Guided by 3D Correlative Microscopy. Biophys J 110, 860-869.

Asano, S., Fukuda, Y., Beck, F., Aufderheide, A., Forster, F., Danev, R., Baumeister, W., 2015. A molecular census of 26S proteasomes in intact neurons. Science 347, 439-442.

Aufderheide, A., Beck, F., Stengel, F., Hartwig, M., Schweitzer, A., Pfeifer, G., Goldberg, A.L., Sakata, E., Baumeister, W., Forster, F., 2015. Structural characterization of the interaction of Ubp6 with the 26S proteasome. Proc Natl Acad Sci U S A 112, 8626-8631.

Bartesaghi, A., Merk, A., Banerjee, S., Matthies, D., Wu, X., Milne, J.L., Subramaniam, S., 2015. 2.2 A resolution cryo-EM structure of beta-galactosidase in complex with a cell-permeant inhibitor. Science 348, 1147-1151.

Bernecky, C., Herzog, F., Baumeister, W., Plitzko, J.M., Cramer, P., 2016. Structure of transcribing mammalian RNA polymerase II. Nature 529, 551-554.

Cheng, Y.F., 2015. Single-Particle Cryo-EM at Crystallographic Resolution. Cell 161.

Danev, R., Nagayama, K., 2010. Phase plates for transmission electron microscopy. Methods in enzymology 481, 343-369.

Danev, R., Baumeister, W., 2016. Cryo-EM single particle analysis with the Volta phase plate. Elife.

Danev, R., Buijsse, B., Khoshouei, M., Plitzko, J.M., Baumeister, W., 2014. Volta potential phase plate for in-focus phase contrast transmission electron microscopy. Proc Natl Acad Sci U S A 111, 15635-15640.

Daum, B., Nicastro, D., Austin, J., 2nd, McIntosh, J.R., Kuhlbrandt, W., 2010. Arrangement of photosystem II and ATP synthase in chloroplast membranes of spinach and pea. The Plant cell 22, 1299-1312.

Davies, K.M., Strauss, M., Daum, B., Kief, J.H., Osiewacz, H.D., Rycovska, A., Zickermann, V., Kuhlbrandt, W., 2011. Macromolecular organization of ATP synthase and complex I in whole mitochondria. Proc Natl Acad Sci U S A 108, 14121-14126.

Engel, B.D., Schaffer, M., Cuellar, L.K., Villa, E., Plitzko, J.M., Baumeister, W., 2015a. Native architecture of the Chlamydomonas chloroplast revealed by in situ cryo-electron tomography. Elife 4.

Engel, B.D., Schaffer, M., Albert, S., Asano, S., Plitzko, J.M., Baumeister, W., 2015b. In situ structural analysis of Golgi intracisternal protein arrays. Proc Natl Acad Sci U S A 112, 11264-11269.

Forster, F., Han, B.G., Beck, M., 2010. Visual proteomics. Methods in enzymology 483, 215-243.

Frank, J., 2006. Three-dimensional electron microscopy of macromolecular assemblies : visualization of biological molecules in their native state. 2nd ed. Oxford University Press, Oxford ; New York.

Fukuda, Y., Laugks, U., Lucic, V., Baumeister, W., Danev, R., 2015. Electron cryotomography of vitrified cells with a Volta phase plate. J Struct Biol 190, 143-154.

Glaeser, R.M., 2013. Invited review article: Methods for imaging weak-phase objects in electron microscopy. The Review of scientific instruments 84, 111101.

Grimm, R., Barmann, M., Hackl, W., Typke, D., Sackmann, E., Baumeister, W., 1997. Energy filtered electron tomography of ice-embedded actin and vesicles. Biophysical Journal 72, 482-489.

Hagen, C., Dent, K.C., Zeev-Ben-Mordehai, T., Grange, M., Bosse, J.B., Whittle, C., Klupp, B.G., Siebert, C.A., Vasishtan, D., Bauerlein, F.J., Cheleski, J., Werner, S., Guttmann, P., Rehbein, S., Henzler, K., Demmerle, J., Adler, B., Koszinowski, U., Schermelleh, L., Schneider, G., Enquist, L.W., Plitzko, J.M., Mettenleiter, T.C., Grunewald, K., 2015. Structural Basis of Vesicle Formation at the Inner Nuclear Membrane. Cell 163, 1692-1701.

Harapin, J., Bormel, M., Sapra, K.T., Brunner, D., Kaech, A., Medalia, O., 2015. Structural analysis of multicellular organisms with cryo-electron tomography. Nat Methods.

Hayles, M.F., Stokes, D.J., Phifer, D., Findlay, K.C., 2007. A technique for improved focused ion beam milling of cryo-prepared life science specimens. J Microsc 226, 263-269.

Hsieh, C., Schmelzer, T., Kishchenko, G., Wagenknecht, T., Marko, M., 2014. Practical workflow for cryo focused-ion-beam milling of tissues and cells for cryo-TEM tomography. J Struct Biol 185, 32-41.

Khoshouei, M., Pfeffer, S., Baumeister, W., Förster, F., Danev, R., 2016. Subtomogram analysis using the Volta phase plate. J Struct Biol.

Kremer, J.R., Mastronarde, D.N., McIntosh, J.R., 1996. Computer visualization of three-dimensional image data using IMOD. J Struct Biol 116, 71-76.

Kuhlbrandt, W., 2014. Biochemistry. The resolution revolution. Science 343, 1443-1444.

Langford, R.M., 2006. Focused ion beam nanofabrication: a comparison with conventional processing techniques. Journal of nanoscience and nanotechnology 6, 661-668.

Li, S., Fernandez, J.J., Marshall, W.F., Agard, D.A., 2012. Three-dimensional structure of basal body triplet revealed by electron cryo-tomography. EMBO J 31, 552-562.

Li, X., Mooney, P., Zheng, S., Booth, C.R., Braunfeld, M.B., Gubbens, S., Agard, D.A., Cheng, Y., 2013. Electron counting and beam-induced motion correction enable near-atomic-resolution single-particle cryo-EM. Nat Methods 10, 584-590.

Lucic, V., Rigort, A., Baumeister, W., 2013. Cryo-electron tomography: the challenge of doing structural biology in situ. J Cell Biol 202, 407-419.

Mahamid, J., Schampers, R., Persoon, H., Hyman, A.A., Baumeister, W., Plitzko, J.M., 2015. A focused ion beam milling and lift-out approach for site-specific preparation of frozen-hydrated lamellas from multicellular organisms. J Struct Biol 192, 262-269.

Mahamid, J., Pfeffer, S., Schaffer, M., Villa, E., Danev, R., Cuellar, L.K., Forster, F., Hyman, A.A., Plitzko, J.M., Baumeister, W., 2016. Visualizing the molecular sociology at the HeLa cell nuclear periphery. Science 351, 969-972.

Marko, M., Hsieh, C., Schalek, R., Frank, J., Mannella, C., 2007. Focused-ion-beam thinning of frozen-hydrated biological specimens for cryo-electron microscopy. Nat Methods 4, 215-217.

Mastronarde, D.N., 2005. Automated electron microscope tomography using robust prediction of specimen movements. J Struct Biol 152, 36-51.

Medalia, O., Weber, I., Frangakis, A.S., Nicastro, D., Gerisch, G., Baumeister, W., 2002. Macromolecular architecture in eukaryotic cells visualized by cryoelectron tomography. Science 298, 1209-1213.

Nans, A., Kudryashev, M., Saibil, H.R., Hayward, R.D., 2015. Structure of a bacterial type III secretion system in contact with a host membrane in situ. Nat Commun 6, 10114.

Ortiz, J.O., Forster, F., Kurner, J., Linaroudis, A.A., Baumeister, W., 2006. Mapping 70S ribosomes in intact cells by cryoelectron tomography and pattern recognition. J Struct Biol 156, 334-341.

Pfeffer, S., Burbaum, L., Unverdorben, P., Pech, M., Chen, Y., Zimmermann, R., Beckmann, R., Forster, F., 2015. Structure of the native Sec61 protein-conducting channel. Nat Commun 6, 8403.

Pigino, G., Bui, K.H., Maheshwari, A., Lupetti, P., Diener, D., Ishikawa, T., 2011. Cryoelectron tomography of radial spokes in cilia and flagella. J Cell Biol 195, 673-687.

Rigort, A., Baeuerlein, F.J.B., Villa, E., Eibauer, M., Laugks, T., Baumeister, W., Plitzko, J.M., 2012. Focused ion beam micromachining of eukaryotic cells for cryo-electron tomography. Proc Natl Acad Sci U S A 109, 4449-4454.

Rigort, A., Bäuerlein, F., Laugks, T., Hayles, M., Mathisen, C., Lich, B., Morrison, R., Leis, A., Baumeister, W., Plitzko, J.M., 2010a. A 360º Rotatable Cryo-FIB Stage for Micromachining Frozen-Hydrated Specimens for Cryo-Electron Tomography. Microscopy and Microanalysis 16(Suppl. 2), pp 220-221.

Rigort, A., Bauerlein, F.J.B., Leis, A., Gruska, M., Hoffmann, C., Laugks, T., Bohm, U., Eibauer, M., Gnaegi, H., Baumeister, W., Plitzko, J.M., 2010b. Micromachining tools and correlative approaches for cellular cryo-electron tomography. J Struct Biol 172, 169-179.

Schaffer, M., Schaffer, B., Ramasse, Q., 2012. Sample preparation for atomic-resolution STEM at low voltages by FIB. Ultramicroscopy 114, 62-71.

Schaffer, M., Engel, B.D., Laugks, T., Mahamid, J., Plitzko, J.M., Baumeister, W., 2015. Cryo-focused Ion Beam Sample Preparation for Imaging Vitreous Cells by Cryo-electron Tomography. Bio-protocol 5, e1575.

Schur, F.K., Hagen, W.J., Rumlova, M., Ruml, T., Muller, B., Krausslich, H.G., Briggs, J.A., 2015. Structure of the immature HIV-1 capsid in intact virus particles at 8.8 A resolution. Nature 517, 505-508.

Strunk, K.M., Wang, K., Ke, D., Gray, J.L., Zhang, P., 2012. Thinning of large mammalian cells for cryo-TEM characterization by cryo-FIB milling. J Microsc 247, 220-227.

Umen, J.G., Goodenough, U.W., 2001. Control of cell division by a retinoblastoma protein homolog in Chlamydomonas. Genes Dev 15, 1652-1661.

von Appen, A., Kosinski, J., Sparks, L., Ori, A., DiGuilio, A.L., Vollmer, B., Mackmull, M.T., Banterle, N., Parca, L., Kastritis, P., Buczak, K., Mosalaganti, S., Hagen, W., Andres-Pons, A., Lemke, E.A., Bork, P., Antonin, W., Glavy, J.S., Bui, K.H., Beck, M., 2015. In situ structural analysis of the human nuclear pore complex. Nature 526, 140-143.

Zhou, A., Rohou, A., Schep, D.G., Bason, J.V., Montgomery, M.G., Walker, J.E., Grigorieff, N., Rubinstein, J.L., 2015. Structure and conformational states of the bovine mitochondrial ATP synthase by cryo-EM. Elife 4, e10180.

# Supplementary materials

## Technical considerations associated with cryo-FIB

### 1. Temperatures

Sufficiently low cryogenic temperatures must be ensured throughout sample handling, transfers and FIB milling to avoid devitrification of the specimen. In particular, the possibility of heat transfer during metal coating, organometallic Pt deposition and the ion milling process, as well as the temperature gradient between the position of the temperature sensor on the cryo-stage and the sample position need to be considered. Cooling of the FIB stage to at least 20 °C below -134 °C (the ice phase transition temperature) has reliably provided stable working conditions covering these additional uncertainties. In addition, sample-handling tools must be appropriately cooled to cryogenic temperature before they come into contact with the sample.

### 2. Vacuum in the microscope chamber

It is essential to avoid water vapor deposition on the lamella during the FIB work and subsequent transfers. While a vacuum level of $5x10^{-6}$ mbar in the FIB chamber is a minimum requirement, the relative humidity in the chamber strongly influences contamination growth rates. Growth rates of 15 nm/hour or less can be regularly achieved with chamber vacuum levels of $2x10^{-7}$ mbar. However, as dual-beam FIB microscopes are generally not built as high vacuum instruments, ensuring such working conditions is challenging. Several factors affect chamber vacuum and contamination growth: the humidity in the microscope room, the transfer time during which the transfer airlock is open, the vacuum level in the airlock, the period since the last chamber venting to atmosphere, the tightness of all seals in the FIB chamber, the tightness of the tubing connection for an open nitrogen circuit-cooled cryo-stage and the water content in the open nitrogen circuit.

Surface contamination deposited in the FIB chamber forms a fine-grained homogenous layer that is not easily recognized in single projection images (Figure S3 A-B) except at the edges of the lamella (Figure S3 C). It is nevertheless detrimental for obtaining high-quality tomograms if it significantly increases the lamella thickness. The thickness of the contamination layer can be measured directly from the reconstructed tomograms. In an x,z tomographic slice, it appears as an additional layer on the lamella surface (Figure 3 D). The contamination appears predominantly on the top surface of the lamella, corresponding to the grid surface that is exposed to the FIB-chamber environment, while the backside is shielded by the cryo-shuttle. By monitoring the cryo-chamber with mass spectrometry, we determined

that the contamination is most likely due to water vapor condensing on the cold sample, despite the presence of a cryo-shield. In the example shown here, the contamination growth rate is estimated to be 45 nm/hr at a chamber vacuum value of $2x10^{-6}$ mbar. These values are given only as rough guides, as variations in relative humidity result in different growth rates at a given vacuum level. To avoid this type of contamination, we constantly monitor the overall vacuum levels and measure the water content in the FIB chamber by mass spectrometry at regular intervals. Small leaks can thus be quickly discovered and sealed, increasing overall reproducibility of sample quality.

However, as stated above, even with a vacuum of $2x10^{-7}$ mbar, water vapor can still condense on lamellas, albeit at a slower rate (< 15 nm/hr). Thus, the finished lamellas should not remain in the FIB chamber for too long. To obtain several lamellas on a single grid, instead of completing one lamella after the other, we perform the final cleaning step for all of the lamellas at the end of the FIB session.

## 3. Transfers

Sample transfer in and out of the FIB chamber requires that the FIB airlock system is pumped below $10^{-6}$ mbar to avoid contamination. This is particularly crucial for unloading of the grids, as transfer at lower vacuum levels can introduce contamination that directly alters the lamella surfaces (e.g. small ice crystals that deteriorate imaging and increase the effective lamella thickness).

Two steps during the subsequent transfers for retrieving the milled grids are critical: 1) While the sample is in the transfer unit, it is not actively cooled or pumped. The vacuum level solely depends on the starting vacuum in the airlock and then degenerates over time without a possibility to measure it. Thus, this step should be completed within 5 min. 2) When the shuttle is finally inserted into the liquid nitrogen, it is exposed to low vacuum for a short time (~$10^{-2}$ mbar at best). Alternatively, some transfer systems can be vented with nitrogen gas.

Figure S4 shows typical examples of contamination on FIB lamellas introduced during transfers after milling, due to either water content in the $LN_2$ used for sample handling (Figure S4 A, D) or exposure to water vapor under insufficient vacuum. The former can be minimized by using dry liquid nitrogen and ensuring that the loading station and handling tools are dry before cooling. The later forms of contamination are clearly visible as layers of variably sized ice crystals. The size and homogeneity of the ice layer are indicative for the type of vacuum leak. Long exposure under a slightly contaminating environment will result in a homogenous layer of small crystals (Figure S4 B, E), whereas sudden, short exposure to a highly contaminating environment will result in large, rough crystals (Figure S4 C, F).

## Supplementary figures

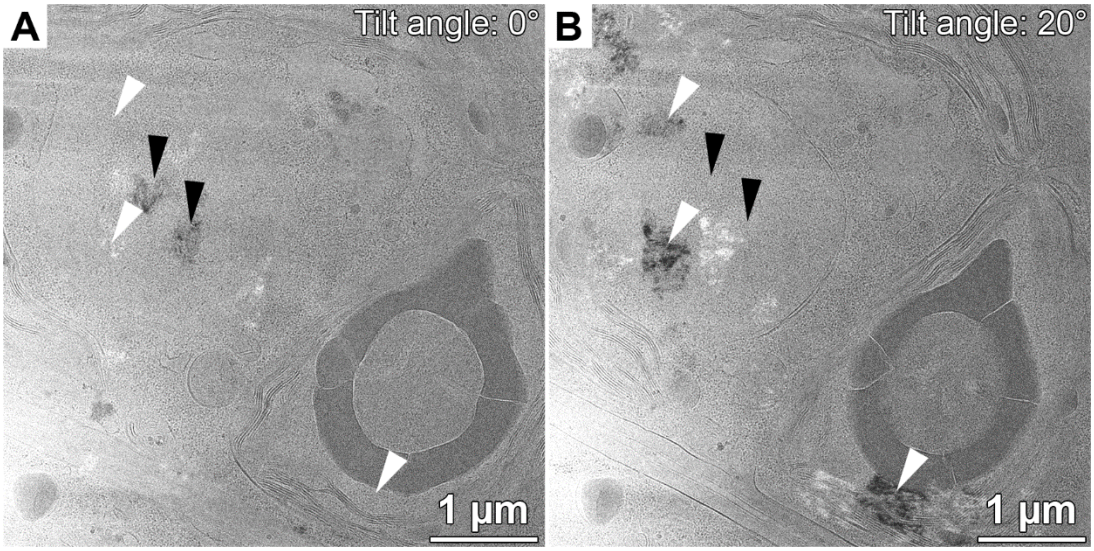


**Figure S1**. Crystalline ice in FIB lamellas caused by incomplete vitrification of *Chlamydomonas* cells. **A** and **B** are images of the same area at different tilt angles. Structural information is obscured by changes in diffraction contrast during tilt-series acquisition caused by the crystalline domains in the sample. Diffraction contrast due to crystalline ice is visible in **A** and not visible in **B** (black arrowheads), while other contrast changes appear in **B** (white arrowheads). Lamella preparation provides access to the inner regions of thick cells (>10 µm) that are less likely to properly vitrify. Thus, adaptation of the vitrification process becomes necessary; Plunge-freezing parameters, such as the cell concentration and the blotting time must be optimized for each cell type under investigation to give a suitable distribution of the material over the grids. Well-suited samples contain either large single cells (as in the case for HeLa cells) or clusters of smaller cells (as in the case for *Chlamydomonas*, see Figure 4) in a single grid square (Villa et al., 2013).

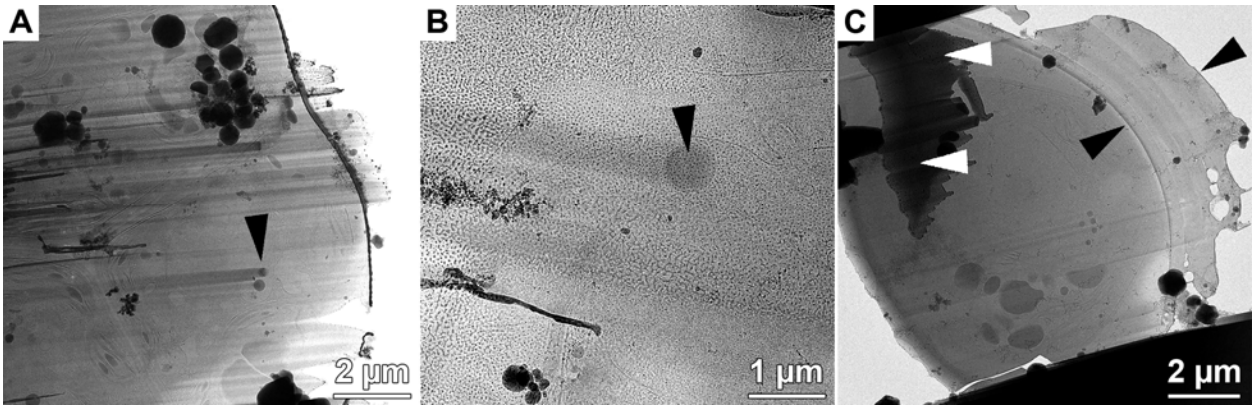


**Figure S2.** Curtaining effects and material redeposition on the lamella surface of *Chlamydomonas* cells. **A:** Lamella with inhomogeneous thickness due to curtaining. Curtaining is caused by differential sputter rates of materials with different densities within the cell. Black arrowheads in A and B indicate a dense lipid droplet causing curtaining. **B:** Material redeposition on the lamella surface (granular texture). **C:** An overly thick organometallic Pt layer (delineated between black arrowheads), which may bend during final milling and cause material redeposition on the lamella surface. White arrowheads show incompletely removed material.

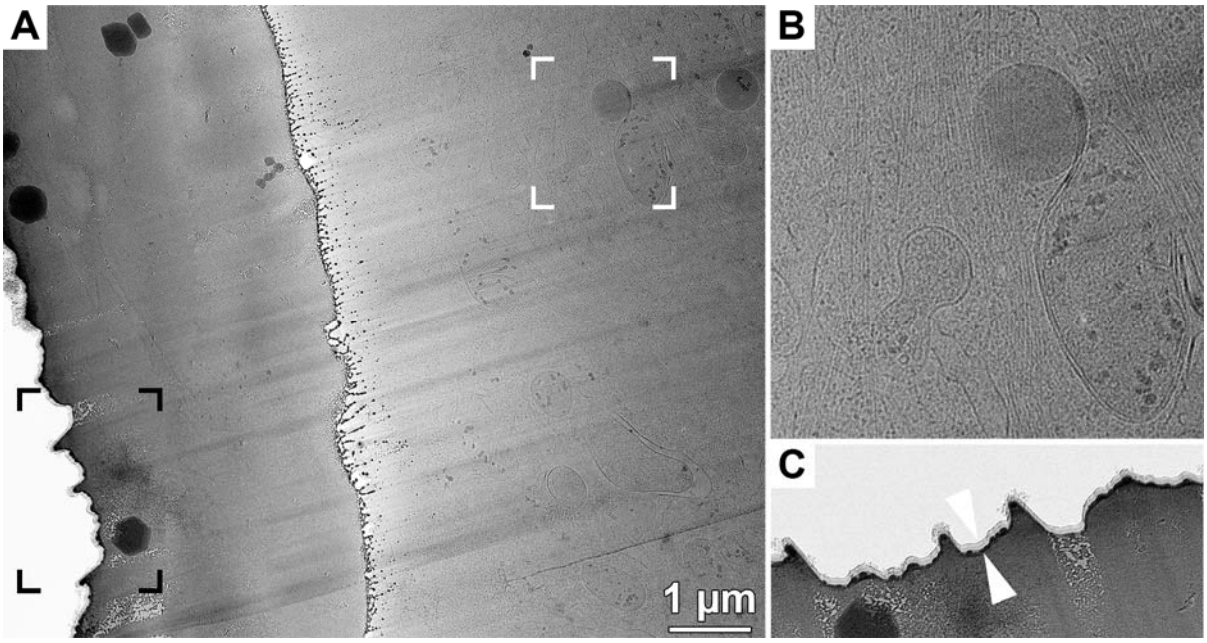


Figure S3. Water vapor deposition in the FIB chamber. A: TEM overview image of a HeLa cell FIB lamella. B: Enlarged view of the white framed area in A. No clear evidence of surface contamination is visible in the projection image, while cellular features are easily observed. C: Enlarged view of the black framed area in A (rotated 90°). A layer of contamination (between the two arrowheads) can be seen extending from the edge of the lamella.

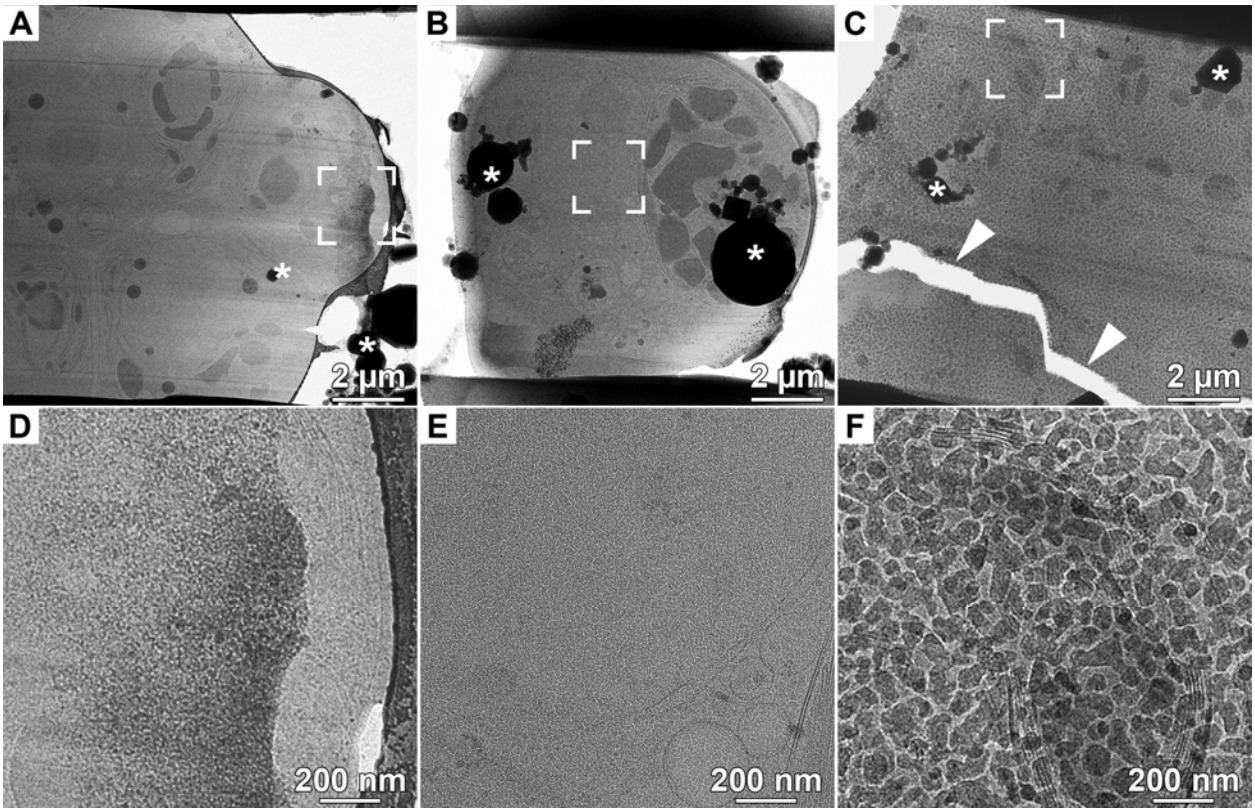


Figure S4. Lamella surface contamination introduced during transfer steps after milling *Chlamydomonas* cells. Large ice crystals are denoted by *. A: Inhomogeneous ice layer deposited during handling in $LN_2$ (framed area is enlarged in D). B: Thin homogenous ice deposition due to prolonged exposure to a contaminating environment (framed area is enlarged in E). C: Thick homogenous ice layer deposited due to short exposure to a highly contaminating environment (framed area is enlarged in F). Arrowhead denotes a crack in the lamella produced during sample handling, which reduces the lamella's mechanical support and causes vibrations and drift during cryo-ET.

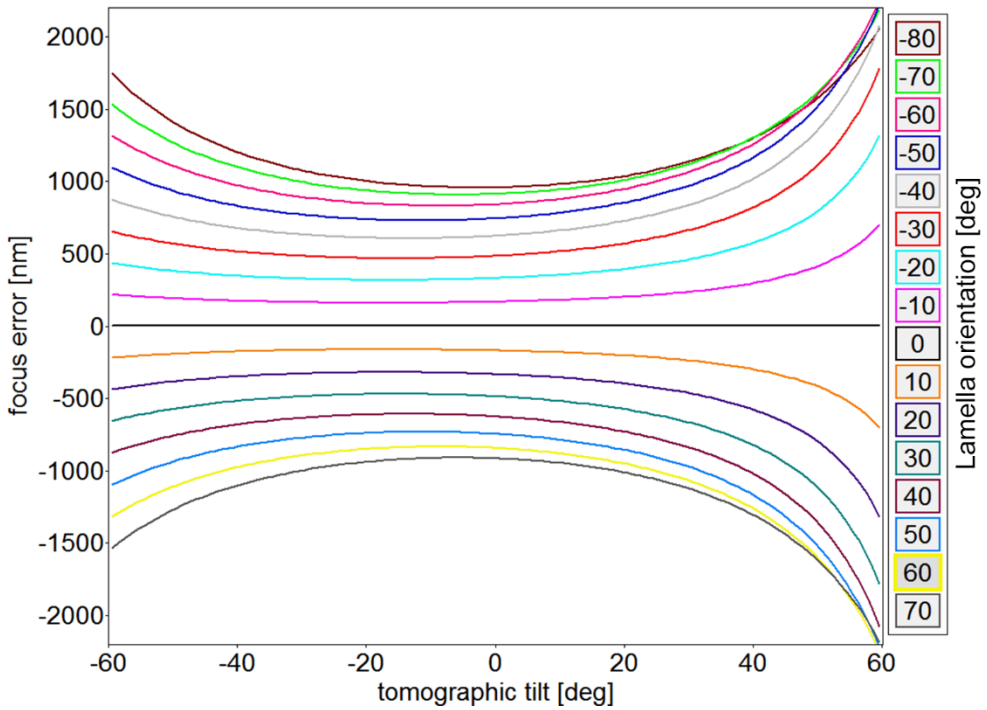


Figure S5. Model calculations of focus errors as a function of the tomographic tilt angle and the angle of the lamella orientation relative to the tilt axis (see Figure 8). The values in this plot were calculated for a tilt-series with an 18° lamella pre-tilt (maximum pre-tilt used in this study) and 3 μm separation between the focus and exposure areas.